

Unexpected Marangoni Condensation in Negative Binary Mixtures

Abenezer Abere¹, Patricia B. Weisensee^{1,2,}*

¹Department of Mechanical Engineering & Materials Science, Washington University in St.

Louis, St. Louis, Missouri 63130, USA

²Institute of Materials Science and Engineering, Washington University in St. Louis, St. Louis,

Missouri 63130, USA

KEYWORDS: Mixtures, Thermo-diffusion, Film instability, Marangoni condensation, Enhanced heat transfer

ABSTRACT

Marangoni condensation—where surface tension gradients induce instabilities that lead to condensate film breakup into discrete droplets—has traditionally been thought of being restricted to “positive” binary mixtures, where the less volatile component has higher surface tension. “Negative” mixtures were expected to exhibit stable filmwise condensation. Here, we demonstrate unexpected spontaneous Marangoni-driven pseudo-dropwise condensation in “negative” water–ethylene glycol and water–triethylene glycol mixtures. Strong thermo-diffusion in these dilute mixtures enables preferential glycol enrichment in colder condensate film regions during

condensation, generating surface tension gradients that trigger film breakup, leading to $>6\times$ wettability-independent heat transfer enhancement compared to filmwise condensation. Our work challenges the conventional framework that restricts Marangoni condensation to "positive mixtures"—a superficial classification that oversimplifies the underlying interfacial mechanisms that can trigger robust Marangoni condensation, offering new pathways for enhancing phase change heat transfer in industrial applications without the need for expensive and degradation-prone surface coatings.

INTRODUCTION

Condensation, a ubiquitous phase change phenomenon, plays a central role in power generation, heating, ventilation, and air conditioning (HVAC) systems, thermal management, desalination, and atmospheric water harvesting technologies [1–5]. The efficiency of these processes is determined by the condensation mode. In filmwise condensation, a thick liquid layer covers the entire condensing surface, which acts as thermal resistance that hinders efficient heat transfer [6,7]. In contrast, dropwise condensation is characterized by discrete droplets that continually nucleate, grow, and shed the surface by gravity or vapor shear [7,8]. Dropwise condensation can enhance heat and mass transfer by more than an order of magnitude compared with its filmwise counterpart [7,8], but usually requires surface functionalization [1,9–13]. Although initially effective, the applied coatings face significant challenges in durability and reliability [14–18], making them unsuitable for long-term industrial applications [12,14,15,19].

Alternatively, condensation enhancement can be achieved by leveraging interfacial instabilities that arise from the fluid properties of multicomponent fluid systems rather than surface modifications. During the condensation of vapor mixtures, naturally occurring temperature and

composition inhomogeneities can create surface tension gradients along the condensing liquid interface [20–23]. The resulting surface tension gradient induces spontaneous Marangoni convection within the condensate film and initiates interfacial instability [20–23]. This instability can grow and break the condensate film into a set of discrete droplets, independent of the substrate's wettability [20–22]. This Marangoni-driven instability is a passive and self-sustaining mechanism that resembles a quasi-dropwise condensation mode without the need of substrate modifications. Despite the fundamentally different mechanism of droplet formation compared to traditional dropwise condensation, Marangoni condensation can sustain up to 10-fold enhancements in heat transfer performance compared to filmwise condensation; very similar to wettability-driven dropwise condensation [21,22,24–26].

Historically, the occurrence of Marangoni condensation of binary vapors has been explained by the relationship between the surface tension and volatility of the two components and the resulting sign of the surface tension gradient on the condensing film [22,23]. Generally, the change in surface tension with respect to the film thickness must be positive for any film instabilities to grow and ultimately to break up into individual droplets. It is thought that a mixture must be “positive” (for example, a water-ethanol mixture), meaning the surface tension of the high boiling point component (*e.g.*, water) must be higher than the surface tension of the component with the lower boiling point (*e.g.*, ethanol) [23]. Some azeotropic mixtures can also locally satisfy the instability criterion [26,27]. In contrast, a “negative” non-azeotropic mixture (*e.g.*, water-ethylene glycol), for which the surface tension of the high boiling component (ethylene glycol) is lower than that of the more volatile component (water), is thought to stabilize the film and impede any occurrence of pseudo-dropwise Marangoni condensation [21–23].

In this letter we show that this historical framework is incomplete at best and incorrect at worst. Through a combination of experimentation and macroscopic interfacial thermodynamic modeling using water-glycol mixtures as exemplary “negative” systems, we propose that thermo-diffusion drives local compositional gradients that destabilize the condensate film, triggering spontaneous and robust droplet formation, motion, and shedding, irrespective of the substrate wettability. When a temperature gradient is imposed on dilute water-glycol mixtures, as is the case for condensation on a cooled substrate, thermo-diffusion drives the heavier glycol molecules from warmer toward colder regions, enriching the thinner (and cooler) areas of the uneven condensate film with glycol [28–30]. This migration changes the interfacial composition and modifies the local surface tension, such that compositional gradients may oppose stabilizing thermal gradients, leading to the growth of film instabilities and eventual breakup into individual droplets [21–23]. Thus, we show that even systems nominally classified as “negative” mixture can exhibit spontaneous Marangoni condensation. These findings reveal a new pathway for achieving sustained pseudo-dropwise condensation without being limited to the use of surface coatings or the traditional “positive” mixtures by leveraging intrinsic molecular coupling effects in binary mixtures.

MECHANISTIC UNDERSTANDING OF MARANGONI CONDENSATION

Initially, Marangoni condensation starts out similar to filmwise condensation, that is, with the formation of a thin condensate film covering the cooled substrate. Natural variations in film thickness create temperature inhomogeneities along the film interface. In “positive” systems, such as water–ethanol mixtures [20,22], colder troughs preferentially accumulate the more volatile component, *i.e.*, the component with higher vapor pressure, generating concentration gradients that induce surface tension gradients (see Figure 1(a)). These gradients drive Marangoni flows from regions of lower to higher surface tension, thus causing the growth of a film instability that results

in the formation of individual droplets. The onset of instability can be expressed by the necessary, but not sufficient condition [23]:

$$\frac{\partial \sigma}{\partial \delta} \equiv \left(\frac{\partial \sigma}{\partial T} \right)_{sat} \left(\frac{\partial T}{\partial \delta} \right) > 0, \quad \text{Eq. (1)}$$

where σ is the local surface tension of the liquid mixture, δ is the local film thickness, T is the local interfacial temperature, and the subscript *sat* represents local saturation conditions. For the cooled condensing surface, $\frac{\partial T}{\partial \delta} > 0$ due to conduction through the film. Therefore, $\frac{\partial \sigma}{\partial T}$ must be greater than zero to satisfy the instability condition in Eq. (1) for Marangoni condensation to occur.

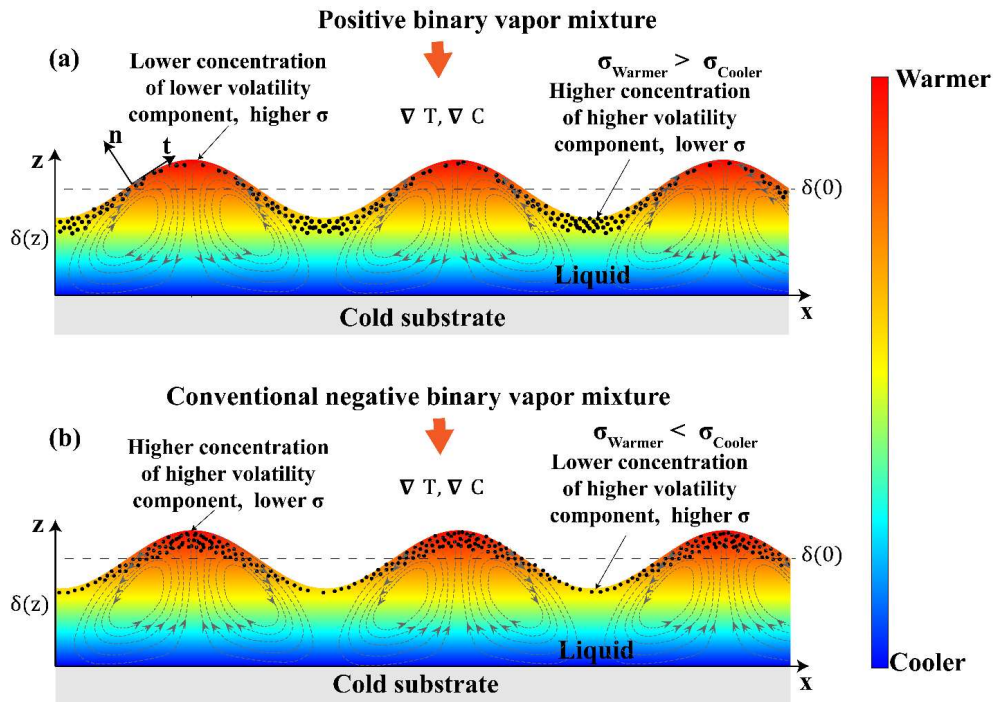


Figure 1. (a) Sketch of a perturbed thin condensate film for a “positive” system, such as a water-ethanol mixture: The resultant temperature gradient causes the colder valley region to have a higher concentration of the more volatile component, in this case ethanol, than the warmer ridge, leading to a lower surface tension in the cooler region ($\sigma_{valley} = \sigma_{cooler} < \sigma_{ridge} = \sigma_{warmer}$). The surface tension gradient leads to Marangoni flow from the valley to the ridge, enhancing the fluid dynamic instability, until the film eventually breaks up to form droplets. (b) Sketch of the historical understanding of a perturbed thin film for a “negative” system, such as water-ethylene glycol. The temperature gradient causes the warmer ridge to have a higher concentration of the less volatile ethylene glycol than the colder valley, leading to a lower surface tension on the ridge ($\sigma_{valley=cool} > \sigma_{ridge=warmer}$). Marangoni convection transports liquid from the ridge to the valley, stabilizing the film. Sketches are not drawn to scale.

In “negative” systems like water–ethylene glycol mixtures, the less volatile component has the lower surface tension. The colder regions in the troughs should hence lead to a higher accumulation of the more volatile component (here: water), whereas the warmer ridges would have a relatively lower percentage of the volatile component (see Figure 1(b)). Because ethylene glycol has a lower surface tension than water, and surface tension generally decreases with temperature, the colder regions are expected to have a higher surface tension than the warmer regions. According to the conventional stability criterion Eq. (1), this should stabilize the condensate film, as the surface tension gradient opposes the direction needed for instability growth and Marangoni convection points from the ridge to the valley. Hence, no Marangoni condensation should occur.

However, contrary to the expectation, water–ethylene glycol (EG) and water–triethylene glycol (TEG) mixtures do exactly that: they condense in a pseudo-dropwise manner, as shown in Figure 2 for condensation of water–EG and water–TEG mixtures at a 1:100 volume ratio on an uncoated copper substrate (root mean square roughness of $R_q \approx 62.1nm$). Details on these visualization experiments are given in the supplemental information (SI), Sections S1-S3, and supplementary videos S1 and S2.

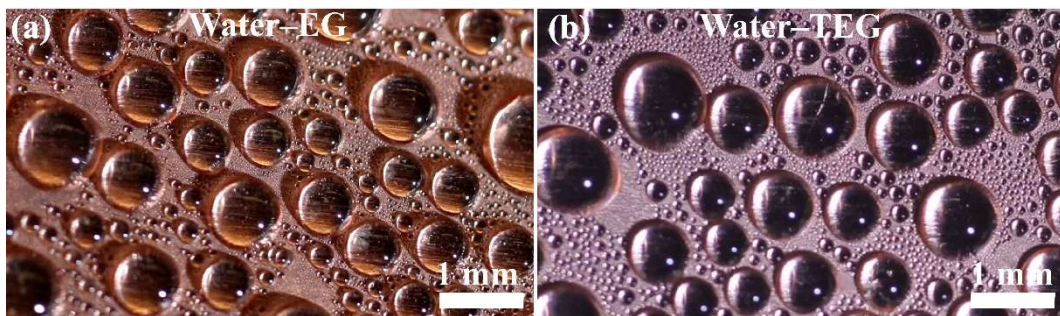


Figure 2. Representative images of fully developed Marangoni-driven pseudo-dropwise condensation modes of (a) a dilute water–EG mixture and (b) a dilute water–TEG mixture, respectively.

These observations raise a fundamental question: Why does such an obvious and pronounced Marangoni response emerge in a negative system that should, according to the traditional framework, favor stable filmwise condensation?

Unlike many aqueous alcohol systems, water–glycol mixtures exhibit a strong coupling between hydrophobic hydration and thermo-diffusion (*i.e.*, Soret effect) [28,30,31]. We propose that the interplay between compositional gradients and thermal diffusion within the perturbed condensing film leads to spontaneous condensate film instabilities in these “negative” binary systems, eventually leading to Marangoni condensation in a system that traditionally has been thought of inevitably exhibiting filmwise condensation on high-surface-energy metallic substrates. To support our hypothesis, we next examine how coupled variations in temperature and composition modify the surface tension and what physical mechanism initiates the surface tension gradients necessary to drive the observed instability growth.

SURFACE TENSION MODELING BASED ON THE VAPOR LIQUID EQUILIBRIUM

To determine the origin of the hydrodynamic instabilities in water–glycol systems, which still have to satisfy the instability criterion of Eq. (1), *i.e.*, $\partial\sigma/\partial T > 0$, but clearly do not follow the traditional “volatility vs. surface tension” framework, we first turn to mapping the interfacial thermodynamic states for a water-ethylene glycol mixture using a vapor liquid equilibrium diagram at 1 bar (see Fig. S4 of the SI for concrete values). Next, we calculate the corresponding temperature- and composition-dependent surface tension of the water–EG mixture (σ_{mix}) with [35] :

$$\sigma_{mix} = \sigma_2(T) - \left(1 + \frac{b(1 - x_1)}{1 - a(1 - x_1)}\right) x_1(\sigma_2(T) - \sigma_1(T)), \quad \text{Eq. (2)}$$

where x_1 denotes the liquid-phase mole fraction of the non-aqueous component ($0 \leq x_1 \leq 1$) and $\sigma_1(T)$ and $\sigma_2(T)$ are the temperature-dependent surface tensions of the non-aqueous

component and pure water, respectively. The dimensionless parameters a and b are obtained by fitting existing surface tension data as a function of composition at a given reference temperature [36].

Water–EG and water–TEG mixtures exhibit a monotonic dependence of surface tension with both temperature and concentration (see SI, Fig. S5). This trend reflects the thermodynamic trajectory of the mixture, since temperature and concentration co-vary along the phase equilibrium path rather than acting as independent variables. To quantify and compare the relative contributions of temperature and composition on surface tension, we evaluate the sensitivity of surface tension to composition ($\partial\sigma/\partial x$) and to temperature ($\partial\sigma/\partial T$) along the vapor liquid equilibrium, as shown in Figure 3 (see SI, Section S6 for details on modeling). We can identify two regimes: the dilute and the concentrated regime. Generally, surface tension is more sensitive to composition than to temperature variations [35]. This is more pronounced in the dilute regime ($x_1 < 0.1$), where slight compositional changes sharply change surface tension gradients compared to higher concentration regions (“concentrated regime”: $x_1 > 0.1$), indicating that the solutal effect is dominant for our condensation experiments. At higher concentration, the magnitude of compositional sensitivity decreases while remaining dominant over the temperature sensitivity. Both composition and temperature sensitivities plateau and remain nearly constant as the composition increases in the concentrated regime.

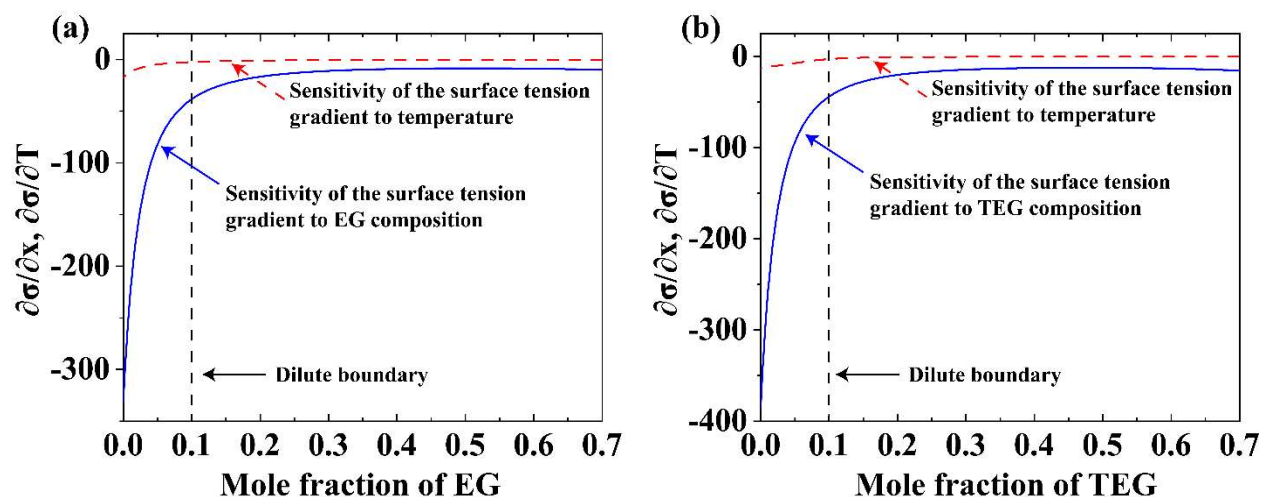


Figure 3. Sensitivity of the surface tension gradient to composition and temperature examined through their respective partial derivatives ($\partial\sigma/\partial x$ and $\partial\sigma/\partial T$, respectively) for (a) a water-EG mixture and (b) a water-TEG mixture. The solid blue line represents the relative magnitude change of the surface tension response to composition, while the dashed red line shows its response to temperature. The vertical broken line differentiates between the dilute and the concentrated regimes.

The pronounced solutal dominance observed in Figure 3 aligns with the underlying molecular mechanisms governing surface tension in the dilute regime. In this region, composition variations disrupt the hydrogen-bond network far more effectively than temperature changes, making solutal effects the principal drivers of interfacial tension gradients and, therefore, interfacial flow. This strong sensitivity of surface tension to composition in the dilute regime can be attributed to distinct molecular interactions, specifically the competition between water-solute and water-water hydrogen bonding [28,37]. These interactions can alter or break the hydrogen bonding between water and solute molecules (EG) [28,31,37–40], leading to significant changes in interfacial thermodynamic properties [37,41,42]. There are two primary mechanisms by which hydrogen bonds between water and solute molecules can be disrupted in aqueous mixtures [28,42]. First, the

addition of a solute with strong affinity for water, such as EG [39], restructures the water hydrogen bond network by forming extensive hydrogen-bonded complexes with water molecules [28,42]. Second, increasing temperature disrupts hydrogen bonding interactions [43]. At higher concentrations, the mixture adopts a new hydrogen-bonded structure, characteristic of glycol-rich phases, reducing the sensitivity of surface tension to composition and temperature.

The local variation in hydrogen bonding—driven by the composition and temperature inhomogeneity—directly control the interfacial surface tension. Any spatial composition non-uniformity induced by the temperature gradients in the condensing film will thus generate surface tension gradients that drive interfacial film instability [22,23]. Hence, this raises the question of which physical mechanism initiates the surface tension gradients necessary to drive the onset of the observed instability during condensation.

MOLECULAR TRANSPORT IN WATER-GLYCOL MIXTURES LEADS TO INSTABILITY GROWTH

During condensation, a temperature gradient arises due to natural variations in condensate film thickness [22,23]. When a water-EG mixture is subjected to a temperature gradient, the molecules do not merely conduct heat, they also migrate due to thermo-diffusion, creating concentration gradients [28,30,44,45]. This phenomenon is quantified by the Soret coefficient, S_T , which characterizes the ratio of thermal diffusion to molecular diffusion in the system [44,45]. The resulting concentration gradient can be expressed as:

$$\nabla c = -S_T x_1(1 - x_1)\nabla T, \quad \text{Eq. (3)}$$

where x is the mole fraction of solute component (EG) and ∇T is the applied temperature gradient. The direction of species migration is determined by the sign of the Soret coefficient: positive values indicate solute migration toward colder regions, whereas a negative value indicates solute migration toward hotter regions.

Water–glycol mixtures show complex and anomalous thermodynamic behavior compared with simpler aqueous alcohols [31,37,46]. This behavior is closely tied to how these mixtures respond to temperature gradients, leading to rich and often pronounced thermo-diffusion effects. In a dilute regime of water-EG mixture, the Soret coefficient is positive and remarkably large ($S_T \approx 20 \times 10^{-3} K^{-1}$ for EG at a mass fraction of ≈ 0.01) [29,30], roughly an order of magnitude higher than that of a water-ethanol mixture at a comparable concentration [29,30]. This underscores the strong compositional sensitivity of thermo-diffusion and the pronounced preference of EG molecules to migrate towards the colder region, reflecting underlying molecular interactions between solute and solvent [28,30].

The water-EG mixture has a positive Soret coefficient [29,30]; thus thermo-diffusion drives EG migration from the warmer to the colder region, leading to EG enrichment in the colder troughs. This compositional redistribution modifies the interfacial composition, which in turn alters the surface tension. Combined with the strong compositional sensitivity of surface tension, this redistribution creates the surface tension gradients necessary to trigger interfacial instability.

Temperature and composition remain intrinsically coupled throughout the condensation process. Notably, the dilute regime in which the compositional sensitivity is maximized (see Figure 3) also coincides with the composition range in which the effect of thermo-diffusion is strongest [28–30]. This coupling reveals a key physical insight: while temperature gradients can directly influence interfacial surface tension through conventional thermodynamic effects (weakening intermolecular forces), their more significant role is to induce composition gradients within the thin condensate film, which then have a much more pronounced effect on surface tension.

For our case of condensation, once the temperature gradient along the undulated thin film is established through heat conduction, EG initially condenses on the film ridges, but then migrates

to the colder regions (see Figure 4(a)) and preferentially accumulates in the troughs (see Figure 4(b)) [28–30]. This solute redistribution reduces surface tension in exactly the region where it would otherwise be higher (*i.e.*, in the cold region of the trough). The resulting surface tension gradient then triggers the Marangoni stress which drives the motion of the condensate liquid film from cooler, EG rich valleys regions toward warmer, EG depleted peaks regions. Ultimately, the induced Marangoni stress along the perturbed condensate-film interface triggers the onset and growth of film instability, causing condensate film breakup into discrete droplets as seen in Figure 2. Thermo-diffusion-driven interfacial motion thus induces interfacial instabilities through coupled thermal-compositional Marangoni flows [47], consistent with the instability mechanism observed here. It is important to note that only the gradient in surface tension, not its absolute value, is relevant to induce an interfacial motion [22].

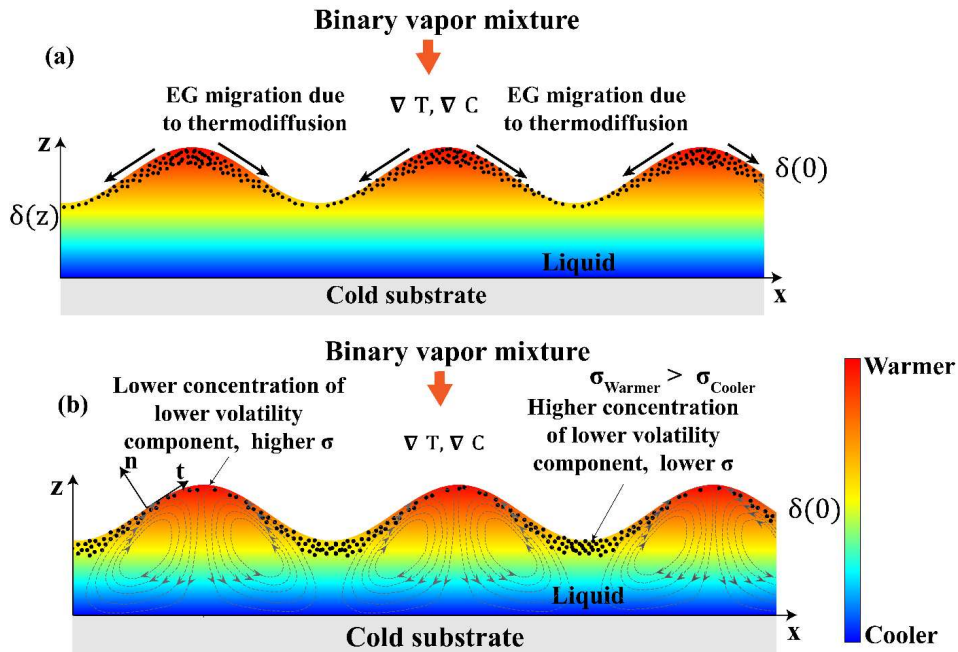


Figure 4. (a) Sketch of a thin perturbed film showing the early stages of water-EG condensation, where EG initially accumulates on the peak region due to its lower volatility compared to water and then migrates towards the cooler region due to thermo-diffusion. (b) Sketch of a perturbed film showing the accumulation of EG in the cooler region due to thermo-diffusion, resulting in the positive surface tension gradient that triggers the film instability to grow. Sketches are not drawn to scale.

ENHANCED CONDENSATION HEAT TRANSFER

Having established that composition gradients in the water-glycol mixture can induce condensate film instability and trigger Marangoni driven dropwise condensation, we next assess whether this mechanism leads to measurable enhancements in thermal performance by examining the heat transfer coefficient as a function of wall subcooling. To determine the improvement of the condensation heat transfer performance, a water-EG mixture is selected as a representative system and tested in a custom-built condensation chamber (see SI sections S7 through S10 for details). Prior to performing the experiment, the vapor is generated by rigorously boiling the mixture to remove non-condensable gases. A high-speed infrared (IR) camera is used to image the condensation process in front view through a sapphire viewport. Time-lapse IR images obtained during the Marangoni dropwise condensation of a water-EG mixture on the clean smooth copper surface show discrete droplet formation, coalescence and gravity-driven shedding (See SI Fig. S11, video S3 and video S4).

Figure 5 shows the measured condensation heat transfer coefficient as a function of surface subcooling (ΔT) for a ≈ 0.55 wt% water-EG mixture undergoing Marangoni dropwise condensation on a smooth copper surface. The measured condensation heat transfer coefficient decreases monotonically with increasing condenser subcooling over the accessible subcooling range $5.6 \leq \Delta T \leq 23$ K. At the lowest measured subcooling, $\Delta T = 5.6$ K, the condensation heat transfer coefficient reaches 114.8 ± 9.7 kW/m²K, corresponding to an enhancement of roughly $6.7 \times$ compared to filmwise condensation of pure steam (≈ 17 kW/m²K). This enhancement arises from the reduced thermal resistance during Marangoni dropwise condensation, where discrete droplets form, coalesce, and shed *via* gravity, sweeping adjacent droplets to expose fresh surface areas which enable the repeated formation of new droplets. As the subcooling increases, the heat

transfer enhancement decreases, yet remains greater than unity even at the highest subcooling tested ($\Delta T \approx 23$ K), demonstrating a broad operational window in which Marangoni-driven dropwise condensation consistently outperforms filmwise condensation, even when the driving temperature difference becomes large.

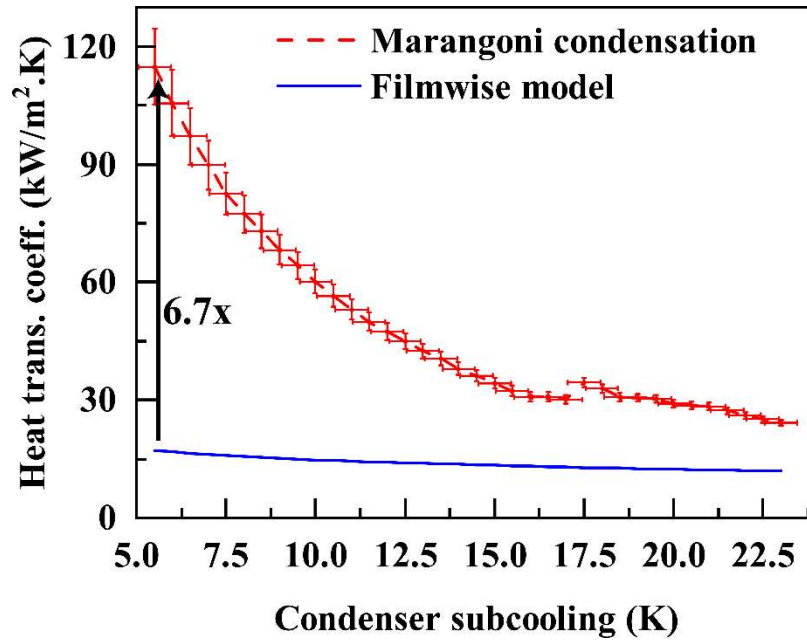


Figure 5. Condensation heat transfer coefficient of a dilute water-EG mixture (≈ 0.55 wt%) as a function of condenser subcooling temperature at a vapor pressure of 52.86 ± 1.62 kPa. The theoretical prediction (solid blue line) represents the Nusselt model for filmwise condensation of pure quiescent water vapor on a bare copper condenser and serves as a baseline case for comparison with the measured condensation heat transfer performance (for model derivation, setup validation and parameters, see SI section S10). The error for the measured condensation heat transfer coefficient was determined by propagating the uncertainty of components associated with measurement (described in detail in the SI section S9) The kink in the data around $\Delta T = 17$ K is due to a slight increase in vapor inflow.

CONCLUSION

This work challenges the conventional framework that limits the Marangoni condensation to “positive mixtures”—a superficial classification that oversimplifies the interfacial liquid-vapor transport physics. We show that in water-EG and water-TEG mixtures, the subtle interfacial coupling of compositional and temperature gradients *via* thermo-diffusion destabilizes condensate films, triggering pseudo-dropwise condensation in systems traditionally expected to form stable

films. These findings reveal that Marangoni condensation is applicable to a wider range of systems beyond traditional “*positive mixture*” criteria. Furthermore, we experimentally demonstrate more than 6x condensation heat transfer performance enhancements compared to filmwise condensation, without the need for any surface modifications, offering new pathways for enhancing condensation performance in industrial applications.

Acknowledgments

This material is based upon work supported by the National Science Foundation under Award No. 2147483.

The authors declare no competing financial interests.

Data availability

The data that support the findings of this article are openly available.

REFERENCES

- [1] A. T. Paxson, J. L. Yagüe, K. K. Gleason, and K. K. Varanasi, Stable Dropwise Condensation for Enhancing Heat Transfer via the Initiated Chemical Vapor Deposition (iCVD) of Grafted Polymer Films, *Advanced Materials* **26**, 418 (2014).
- [2] S. A. Nada, H. F. Elattar, and A. Fouda, Experimental study for hybrid humidification–dehumidification water desalination and air conditioning system, *Desalination* **363**, 112 (2015).
- [3] K.-S. Yang, T.-Y. Yang, C.-W. Tu, C.-T. Yeh, and M.-T. Lee, A novel flat polymer heat pipe with thermal via for cooling electronic devices, *Energy Conversion and Management* **100**, 37 (2015).
- [4] D. Seo, J. Lee, C. Lee, and Y. Nam, The effects of surface wettability on the fog and dew moisture harvesting performance on tubular surfaces, *Sci Rep* **6**, 24276 (2016).
- [5] R. Sathyamurthy, S. A. El-Agouz, and V. Dharmaraj, Experimental analysis of a portable solar still with evaporation and condensation chambers, *Desalination* **367**, 180 (2015).
- [6] E. Schmidt, W. Schurig, and W. Sellschopp, Versuche über die Kondensation von Wasserdampf in Film- und Tropfenform, *Technische Mechanik und Thermodynamik* **1**, 53 (1930).

- [7] V. P. Carey, *Liquid-Vapor Phase-Change Phenomena: An Introduction to the Thermophysics of Vaporization and Condensation Processes in Heat Transfer Equipment*, 3rd ed. (CRC Press, 2020).
- [8] J. W. Rose, Dropwise condensation theory and experiment: A review, *Proceedings of the Institution of Mechanical Engineers, Part A: Journal of Power and Energy* **216**, 115 (2002).
- [9] D. J. Preston, D. L. Mafra, N. Miljkovic, J. Kong, and E. N. Wang, Scalable Graphene Coatings for Enhanced Condensation Heat Transfer, *Nano Lett.* **15**, 2902 (2015).
- [10] J. Ma, H. Cha, M. Kim, D. G. Cahill, and N. Miljkovic, Condensation Induced Delamination of Nanoscale Hydrophobic Films, *Adv Funct Materials* **29**, 1905222 (2019).
- [11] P. B. Weisensee, Y. Wang, H. Qian, D. Schultz, W. P. King, and N. Miljkovic, Condensate droplet size distribution on lubricant-infused surfaces, *International Journal of Heat and Mass Transfer* **109**, 187 (2017).
- [12] J. Sun and P. B. Weisensee, Tailoring wettability to push the limits of condensation, *Current Opinion in Colloid & Interface Science* **67**, 101739 (2023).
- [13] N. Miljkovic, R. Enright, Y. Nam, K. Lopez, N. Dou, J. Sack, and E. N. Wang, Jumping-Droplet-Enhanced Condensation on Scalable Superhydrophobic Nanostructured Surfaces, *Nano Lett.* **13**, 179 (2013).
- [14] J. Xie, J. Xu, X. Li, and H. Liu, Dropwise condensation on superhydrophobic nanostructure surface, Part I: Long-term operation and nanostructure failure, *International Journal of Heat and Mass Transfer* **129**, 86 (2019).
- [15] T. Foulkes et al., Jumping droplets electronics cooling: Promise versus reality, *Applied Physics Letters* **116**, 203701 (2020).
- [16] C. Dorrer and J. R uhe, Some thoughts on superhydrophobic wetting, *Soft Matter* **5**, 51 (2009).
- [17] D. Qu er e, Non-sticking drops, *Rep. Prog. Phys.* **68**, 2495 (2005).
- [18] H. Jo, K. W. Hwang, D. Kim, M. Kiyofumi, H. S. Park, M. H. Kim, and H. S. Ahn, Loss of superhydrophobicity of hydrophobic micro/nano structures during condensation, *Sci Rep* **5**, 9901 (2015).
- [19] D. J. Preston and E. N. Wang, Jumping Droplets Push the Boundaries of Condensation Heat Transfer, *Joule* **2**, 205 (2018).
- [20] J. D. Ford and J. E. Mcaleer, Non-filmwise condensation of binary vapors: Mechanism and droplet sizes, *Can J Chem Eng* **49**, 157 (1971).
- [21] V. V. Mirkovich and R. W. Missen, A study of the condensation of binary vapors of miscible liquids: Part 2: Heat transfer co-efficients for filmwise and non-filmwise condensation, *Can J Chem Eng* **41**, 73 (1963).
- [22] K. Hijikata, Y. Fukasaku, and O. Nakabeppu, Theoretical and Experimental Studies on the Pseudo-Dropwise Condensation of a Binary Vapor Mixture, *Journal of Heat Transfer* **118**, 140 (1996).
- [23] J. D. Ford and R. W. Missen, On the conditions for stability of falling films subject to surface tension disturbances; the condensation of binary vapors, *Can J Chem Eng* **46**, 309 (1968).
- [24] Y. Utaka and S. Wang, Characteristic curves and the promotion effect of ethanol addition on steam condensation heat transfer, *International Journal of Heat and Mass Transfer* **47**, 4507 (2004).
- [25] T. Murase, H. S. Wang, and J. W. Rose, Marangoni condensation of steam-ethanol mixtures on a horizontal tube, *International Journal of Heat and Mass Transfer* **50**, 3774 (2007).
- [26] S. R. Jivani, Investigation of Marangoni Condensation of Binary Mixtures, PhD Thesis, Queen Mary University of London, 2018.

- [27] H. Ohta, S. Yamaguchi, Y. Ito, Y. Shinmoto, and Y. Abe, Nucleate boiling of low-concentration alcohol aqueous solutions for the development of thermal management systems in space, *Microgravity Sci. Technol* **19**, 141 (2007).
- [28] K. Maeda, N. Shinyashiki, S. Yagihara, S. Wiegand, and R. Kita, Ludwig-Soret effect of aqueous solutions of ethylene glycol oligomers, crown ethers, and glycerol: Temperature, molecular weight, and hydrogen bond effect, *The Journal of Chemical Physics* **143**, 124504 (2015).
- [29] K. Maeda, N. Shinyashiki, S. Yagihara, S. Wiegand, and R. Kita, How does thermodiffusion of aqueous solutions depend on concentration and hydrophobicity?, *Eur. Phys. J. E* **37**, 94 (2014).
- [30] C. I. A. V. Santos, M. C. F. Barros, A. C. F. Ribeiro, M. M. Bou-Ali, A. Mialdun, and V. Shevtsova, Transport properties of *n*-ethylene glycol aqueous solutions with focus on triethylene glycol–water, *The Journal of Chemical Physics* **156**, 214501 (2022).
- [31] S. Dixit, J. Crain, W. C. K. Poon, J. L. Finney, and A. K. Soper, Molecular segregation observed in a concentrated alcohol–water solution, *Nature* **416**, 829 (2002).
- [32] Y. Utaka and T. Nishikawa, Measurement of Condensate Film Thickness for Solutal Marangoni Condensation Applying Laser Extinction Method, *J Enh Heat Transf* **10**, 119 (2003).
- [33] A. Oron, S. H. Davis, and S. G. Bankoff, Long-scale evolution of thin liquid films, *Rev. Mod. Phys.* **69**, 931 (1997).
- [34] Y. Utaka and Z. Che, *Condensate Drop Movement by Surface Temperature Gradient on Heat Transfer Surface in Marangoni Dropwise Condensation*, in *An Overview of Heat Transfer Phenomena*, edited by M. S. N. Kazi (InTech, 2012).
- [35] N. Shardt and J. A. W. Elliott, Model for the Surface Tension of Dilute and Concentrated Binary Aqueous Mixtures as a Function of Composition and Temperature, *Langmuir* **33**, 11077 (2017).
- [36] N. B. Vargaftik, B. N. Volkov, and L. D. Voljak, International Tables of the Surface Tension of Water, *Journal of Physical and Chemical Reference Data* **12**, 817 (1983).
- [37] J.-Y. Huot, E. Battistel, R. Lumry, G. Villeneuve, J.-F. Lavallee, A. Anusiem, and C. Jolicoeur, A comprehensive thermodynamic investigation of water-ethylene glycol mixtures at 5, 25, and 45°C, *J Solution Chem* **17**, 601 (1988).
- [38] L. Weng, C. Chen, J. Zuo, and W. Li, Molecular Dynamics Study of Effects of Temperature and Concentration on Hydrogen-Bond Abilities of Ethylene Glycol and Glycerol: Implications for Cryopreservation, *J. Phys. Chem. A* **115**, 4729 (2011).
- [39] A. Kaiser, M. Ritter, R. Nazmutdinov, and M. Probst, Hydrogen Bonding and Dielectric Spectra of Ethylene Glycol–Water Mixtures from Molecular Dynamics Simulations, *J. Phys. Chem. B* **120**, 10515 (2016).
- [40] Y. Wang, F. Li, W. Fang, C. Sun, and Z. Men, Study of hydrogen bonding interactions in ethylene glycol-water binary solutions by Raman spectroscopy, *Spectrochimica Acta Part A: Molecular and Biomolecular Spectroscopy* **260**, 119916 (2021).
- [41] N. G. Tsierkezos and I. E. Molinou, Thermodynamic Properties of Water + Ethylene Glycol at 283.15, 293.15, 303.15, and 313.15 K, *J. Chem. Eng. Data* **43**, 989 (1998).
- [42] O. Syshchuk, D. Afanasenkau, Z. Wang, H. Kriegs, J. Buitenhuis, and S. Wiegand, Influence of temperature and charge effects on thermophoresis of polystyrene beads*, *Eur. Phys. J. E* **39**, 129 (2016).
- [43] N. Zhang, M.-R. Li, and F.-S. Zhang, Structure and dynamics properties of liquid ethylene glycol from molecular dynamics simulations, *Chemical Physics Letters* **718**, 12 (2019).
- [44] C. Ludwig, Difusion awischen ungleich erwärmten Orten gleich zusammengesetzter Lösungen, *Sitz Math Naturwiss Classe Kaiserichen Akad Wiss* **20**, 539 (1856).

- [45] C. Soret, Sur l'état d'équilibre que prend au point de vue de sa concentration une dissolution saline primitivement homogène dont deux parties sont portées a des températures différentes, Arch Sci Phys Nat **2**, 48 (1879).
- [46] P. Wang, J. J. Kosinski, A. Anderko, R. D. Springer, M. M. Lencka, and J. Liu, Ethylene Glycol and Its Mixtures with Water and Electrolytes: Thermodynamic and Transport Properties, Ind. Eng. Chem. Res. **52**, 15968 (2013).
- [47] J. L. Castillo and M. G. Velarde, Thermal diffusion and the Marangoni-Benard instability of a two-component fluid layer heated from below, Physics Letters A **66**, 489 (1978).

Unexpected Marangoni Condensation in Negative Binary Mixtures

Abenezer Abere ¹, Patricia B. Weisensee ^{1,2*}

¹ *Department of Mechanical Engineering & Materials Science, Washington University in St. Louis, St. Louis, Missouri 63130, USA*

² *Institute of Materials Science and Engineering, Washington University in St. Louis, St. Louis, Missouri 63130, USA*

Supplementary Material

*Author to whom correspondence should be addressed.

Patricia B. Weisensee: p.weisensee@wustl.edu.

Contents

S1. Experimental setup for Marangoni condensation visualization	3
S2. Atomic force microscopy (AFM)	4
S3. Visualization of initial droplet formation	5
S4. Phase diagrams of binary mixture systems	6
S5. Surface tension calculation of the binary mixtures	7
S6. Local sensitivity of surface tension	9
S7. Experimental setup for heat transfer measurements	9
S8. Experimental procedure	13
S9. Experimental calculations and error propagation	16
S10. Filmwise condensation model and setup validation	19
S11. Time-resolved IR imaging of Marangoni dropwise condensation	20
References	22

S1. Experimental setup for Marangoni condensation visualization

Figure S1 shows a schematic of the experimental setup that was used for obtaining imaging data (heat transfer and thermal data used a different setup, as described in section S7), consisting of a vapor generator, a cold stage, and an imaging system. The entire setup was housed in a fume hood and the experiments were conducted in the presence of non-condensable gases. This setup was employed for testing whether the binary vapor mixtures would undergo Marangoni condensation. The binary mixtures were prepared according to the ratio specified in the manuscript and physical properties of the corresponding substances are summarized in Table S1.

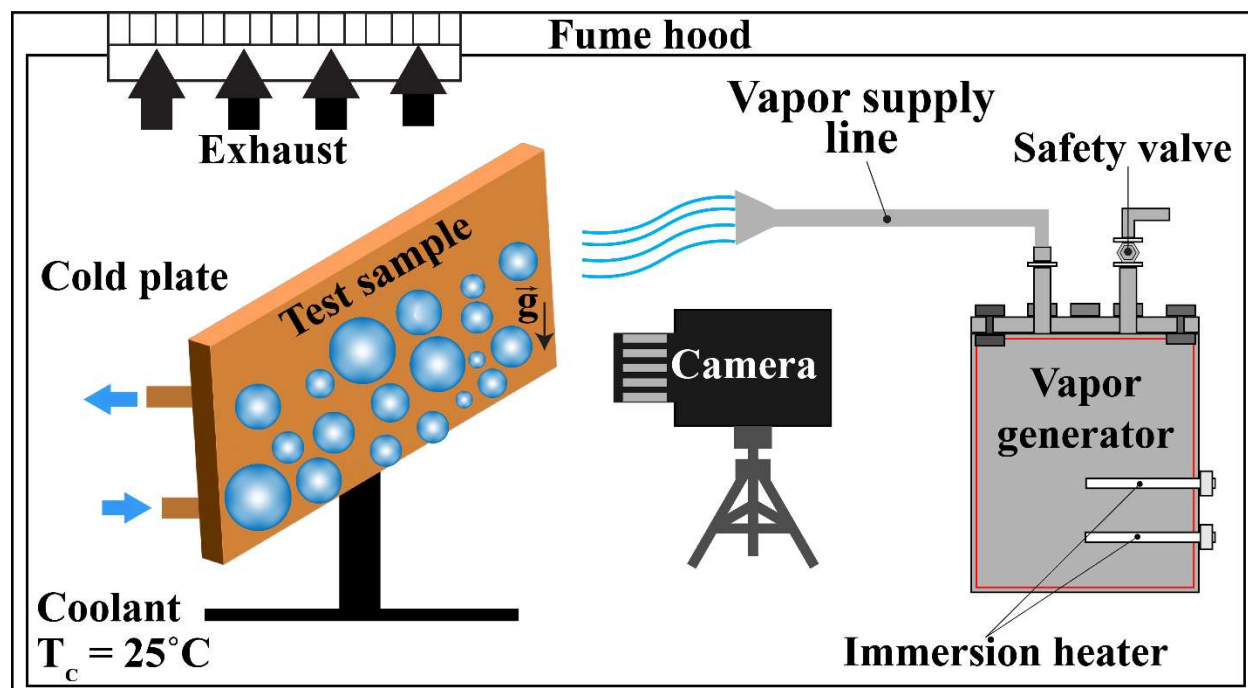


Figure S1. Schematic of the experimental setup for Marangoni condensation demonstration and visualization. Schematics are not drawn to scale.

Table S1. Physical properties of substances used in the experiment

Substance	Supplier	Density (kg/m ³)	Molar mass (g/mol)	Surface tension (mN/m) at 20°C
DI water		997	18.015	72.8
Ethylene glycol (Reagentplus, ≥ 99%)	Sigma-Aldrich	1.113	62.07	48.4
Triethylene glycol (Reagentplus, ≥ 99%)	Sigma-Aldrich	1.124	150.17	45.2

A cylindrical stainless-steel chamber equipped with two immersion cartridge heaters (400W, OEM Heaters) served as a vapor generator. Two separate KF adapter ports were installed on the top of the chamber. The first port was used to attach a bellow angle valve (Kurt J. Lesker) to the vapor generator, which served as a safety vent for over-pressure protection. The second port was connected to a flexible tube that served as the flow line for the incoming vapor mixture, which was channeled towards a condensation surface. A flat copper sample was mounted vertically and secured against the front side a tubed cold plate to serve as condensation surface. A thin layer of thermal paste was applied between the copper sample and the cold plate to ensure good thermal contact. The tubed cold plate was connected to a recirculating chiller (1175PD Recirculating Chiller, VWR Scientific) to supply cooling water at a constant temperature of 25 °C. A DSLR camera (Canon T6i), equipped with a macro lens (Canon MP-E 65mm 1-5x Macro), was used to record the condensation dynamics.

S2. Atomic force microscopy (AFM)

The roughness of the condensing copper substrate was characterized by AFM (Bruker MultiMode) using silicon nitride probes in the ScanAsyst mode. AFM images, as shown in Figure S2, were acquired by scanning areas of 10 μm by 10 μm on the copper surfaces in air under ambient laboratory conditions at a scan rate of 1 Hz. Two images were analyzed with NanoScope Analysis 3.00 software to obtain the root mean square roughness (R_q).

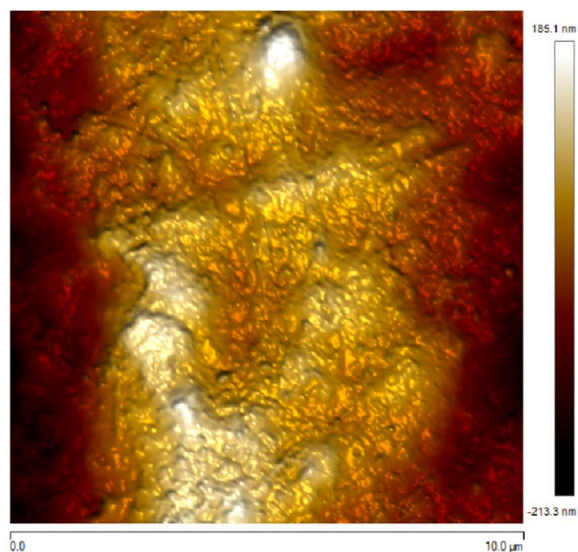


Figure S2. *AFM topography scan of the copper surface used for the experiment.*

S3. Visualization of initial droplet formation

Figure S3(a-c) show a temporal sequence of images during the initial droplet formation stage to capture the full evolution of the condensation mechanism. Upon vapor contact with the copper (see SI, video S1 for initial film dynamics), the surface is quickly covered with a thin continuous liquid film that rapidly destabilizes under surface tension gradient forces¹. As shown in Figure S3 (a), the continuous film develops fine-scale undulations and micro pits—characteristic precursors of Marangoni instability². As the film instability grows, the amplitude of the valleys and the hills grows, and the film undergoes spontaneous breakup along narrow ridges (Figure S3(b)), producing isolated liquid islands that contract into droplets under capillary forces, transitioning the condensation mode to dropwise. Thin residual film patches are still visible between droplets, indicating that the surface undergoes repeated local thinning and film breakup (Figure S3(c)). Finally, Figure S3(d) and (e) show the advanced condensation stages during quasi-steady state operation (copied from Fig. 2 in the main manuscript), where droplets coalesce and translate on the condensing surface. Once these droplets grow large enough, they shed from the surface under gravity, exposing fresh thin film patches that subsequently break again, enabling rapid formation of new droplets.

Overall, the periodic cycle of film spreading, instability growth, condensate film breakup, droplet formation, spontaneous motion of droplets, coalescence, and shedding is highly repeatable, and aligns closely with Marangoni-induced pseudo-dropwise condensation dynamics known from “positive” binary vapor systems³⁻⁵. The same behavior is observed for both tested glycol mixtures (EG and TEG) (see SI, videos S1 and S2), demonstrating that the instability mechanism is robust and independent of surface wettability.

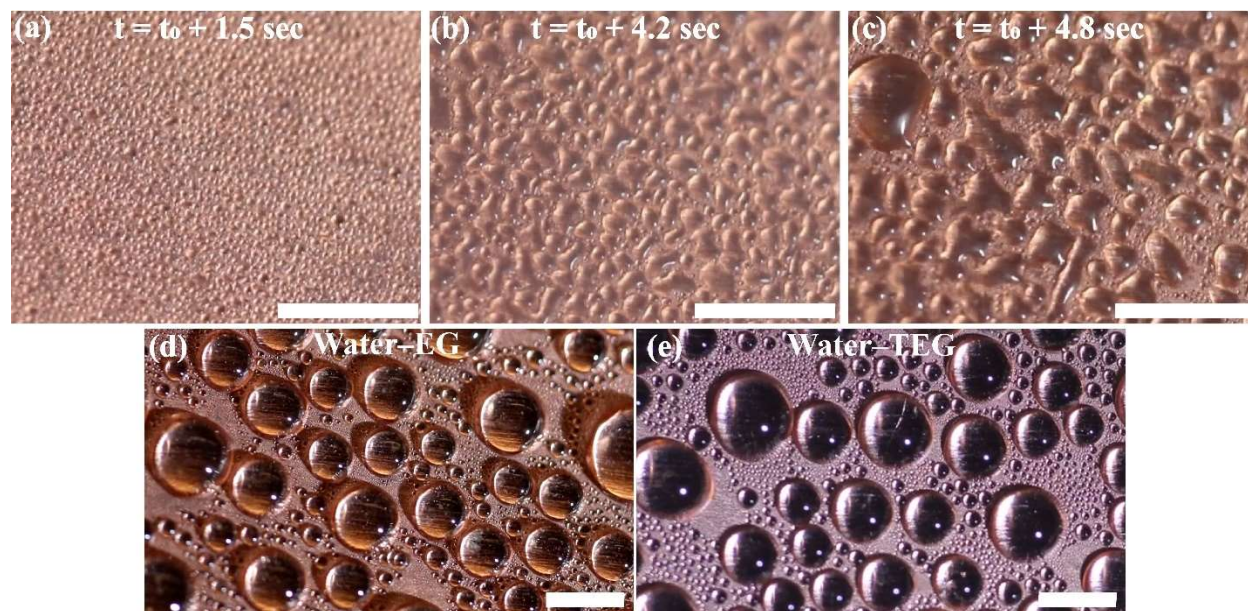


Figure S3. Progression of the condensation process for a water-EG mixture. (a) In early stages, the condensate film develops surface undulations and micro pit features. (b) Later, the thin condensate film breaks up into narrow liquid ridges driven by Marangoni convection. (c) Finally, before fully defined droplets form, irregularly shaped condensate ridges elongate and grow over time. Representative images of fully developed Marangoni-driven pseudo-dropwise condensation modes of (d) a dilute water-EG mixture and (e) a dilute water-TEG mixture, respectively. All scale bars are 1mm.

S4. Phase diagrams of binary mixture systems

The vapor liquid equilibrium (VLE) phase diagrams of the binary systems of water-ethylene glycol and water-triethylene glycol are shown in Figure S4. The red dashed line indicates the vapor line whereas the blue solid line indicates the liquid line. The mixture thermodynamic properties were predicted using the COSMO-RS (Conductor-like Screening Model for Real Solvents) model implementation in the SCM Amsterdam Modeling Suite (AMS2025.1)⁶. COSMO-RS combines quantum-chemically derived molecular surface polarization charge densities with a statistical-thermodynamic treatment of pairwise surface-segment interactions to compute chemical potential and activity coefficients in liquids. These quantities are then used to predict mixture phase equilibria and related thermodynamic properties of binary mixtures. A comprehensive explanation of this model can be found in refs. ^{7,8}.

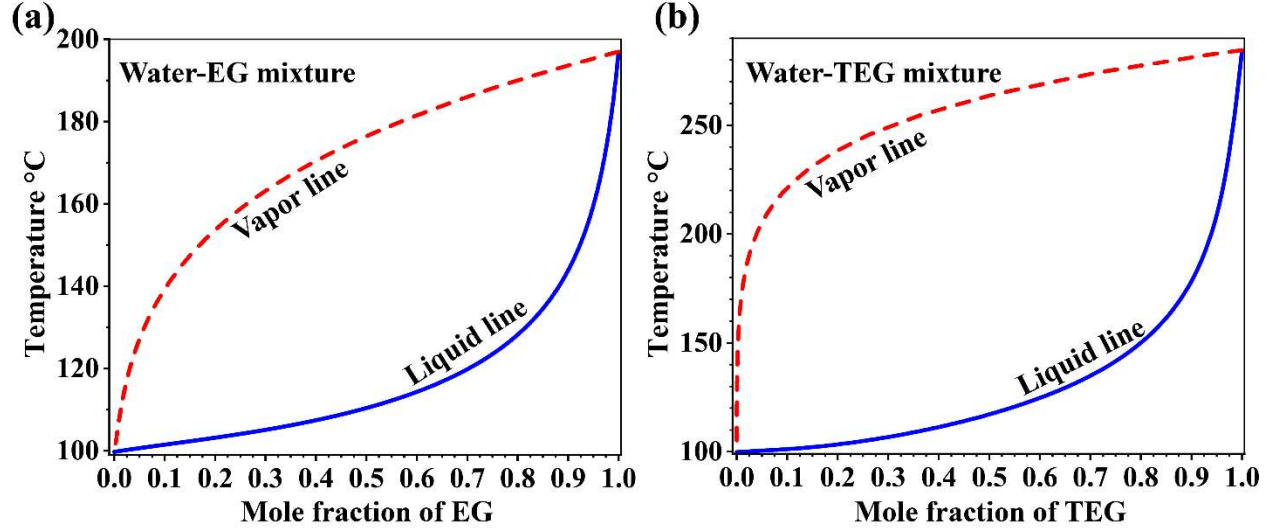


Figure S4. Phase equilibrium diagrams of binary mixtures at 1 bar. (a) Water-ethylene glycol mixture. (b) Water-triethylene glycol mixture. The solid blue lines indicate the liquid line and the red dashed lines indicate the vapor line.

S5. Surface tension calculation of the binary mixtures

Once the composition and temperature data along the VLE is obtained from Figure S4, we use a modified form of the Connors–Wright model to calculate the surface tension of the binary mixtures, as proposed by Shardt *et al.*⁹ and expressed as a function of liquid-phase composition and temperature:

$$\sigma_{mix} = \sigma_2(T) - \left(1 + \frac{b(1 - x_1)}{1 - a(1 - x_1)}\right) x_1 (\sigma_2(T) - \sigma_1(T)), \quad (S1)$$

where x_1 denotes the liquid-phase mole fraction of the non-aqueous component ($0 \leq x_1 \leq 1$), T is the absolute temperature from the VLE phase diagram, $\sigma_2(T)$ and $\sigma_1(T)$ are the surface tensions of pure water and the non-aqueous compound, respectively (mN/m), and the dimensionless parameters a and b are obtained by fitting surface tension data⁹ as a function of composition at a reference temperature chosen to have sufficient experimental points to capture the composition trend.

The surface tension of pure water is calculated as ¹⁰:

$$\sigma_2(T) = 235.8 \left[\frac{T_c - T}{T_c} \right]^{1.256} \left[1 - 0.625 \left(\frac{T_c - T}{T_c} \right) \right], \quad (\text{S2})$$

where $T_c = 647.15\text{K}$ is the critical temperature and T is the absolute temperature from the VLE phase diagram.

The surface tension of ethylene glycol is calculated as ¹¹:

$$\sigma_1(T) = 50.206 - 0.089T, \quad (\text{S3})$$

where T is in $^{\circ}\text{C}$.

The surface tension of triethylene glycol is given by ¹²:

$$\sigma_1(T) = 47.33 - 0.088T, \quad (\text{S4})$$

where T is in $^{\circ}\text{C}$.

Figure S5 shows the calculated variation of surface tension as a function of saturation temperature along the liquid line of the vapor liquid phase equilibria. Note that composition also varies along the temperature axis, in accordance with the equilibrium conditions shown in Figure S4.

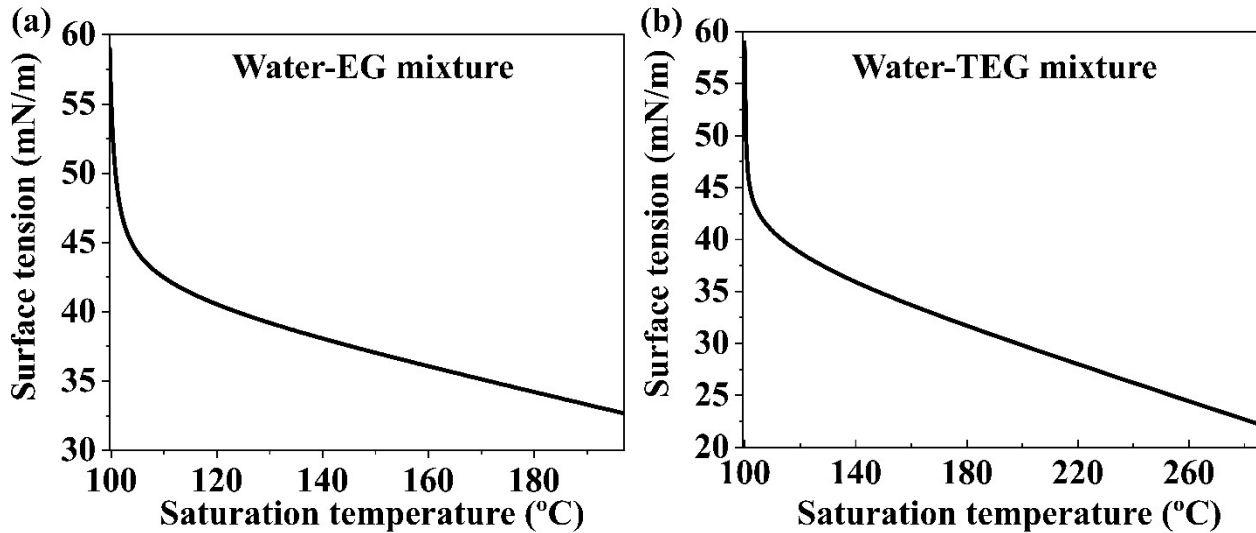


Figure S5. Surface tension of the mixtures as a function of equilibrium temperature (or liquid phase concentration) at the liquid-vapor interface at constant pressure of 1 bar. (a) Water-EG mixture. (b) Water-TEG mixture. The saturation temperature increase on the horizontal axis corresponds to the molar concentration increase of the solute according to the corresponding VLE phase diagram.

S6. Local sensitivity of surface tension

The surface tension of binary mixtures σ_{mix} , as defined in Eq. (S1), is a function of T and x at constant pressure, *i.e.*, $\sigma_{mix} = \sigma(T, x)$ ¹³. The resulting surface tension gradient is sensitive to the variation in temperature and composition along the VLE. Once the surface tension is calculated along the VLE, outlined in section S4, we can quantify the sensitivity of surface tension to composition ($\partial\sigma/\partial x$) and to temperature ($\partial\sigma/\partial T$), which is evaluated along the saturated liquid line of the VLE as¹³:

$$\frac{\partial\sigma}{\partial x} = \left(\frac{\partial\sigma}{\partial x}\right)_T + \left(\frac{\partial\sigma}{\partial T}\right)_x \left(\frac{\partial T}{\partial x}\right)_{sat} \approx \frac{\Delta\sigma}{\Delta x}, \quad (\text{S5})$$

and

$$\frac{\partial\sigma}{\partial T} = \left(\frac{\partial\sigma}{\partial T}\right)_x + \left(\frac{\partial\sigma}{\partial x}\right)_T \left(\frac{\partial x}{\partial T}\right)_{sat} \approx \frac{\Delta\sigma}{\Delta T}, \quad (\text{S6})$$

The data plotted in Figure 3 of the manuscript is calculated using equations (S5) and (S6).

S7. Experimental setup for heat transfer measurements

We used a custom-made condensation chamber for heat transfer measurements with *in-situ* visualization capability, which consists of a vapor generator, a condensation chamber, a vacuum pump, a chilled water bath, and a data acquisition system, as shown in Figure S6.

A custom-built cylindrical stainless steel vapor generator (Ancorp), wrapped with two rope heaters (0.83kW and 0.62kW, Omega), was controlled by two independent Variac power controllers (3PN1010 Variac, Staco Energy Products Co.) and served as the vapor generator (see Figure S6). The vapor generator along with the rope heater were insulated externally to minimize heat loss to the environment. A stainless-steel bellow hose (Kurt J. Lesker), serving as the vapor supply line, was fed into the top of the vapor generator *via* a KF adapter port. The vapor supply line was wrapped with a rope heater (1.4kW, Omega), controlled by a Variac power controller (3PN1010 Variac, Staco Energy Products Co.), to prevent condensation at the inside wall and was thermally insulated to limit the heat loss to the environment.

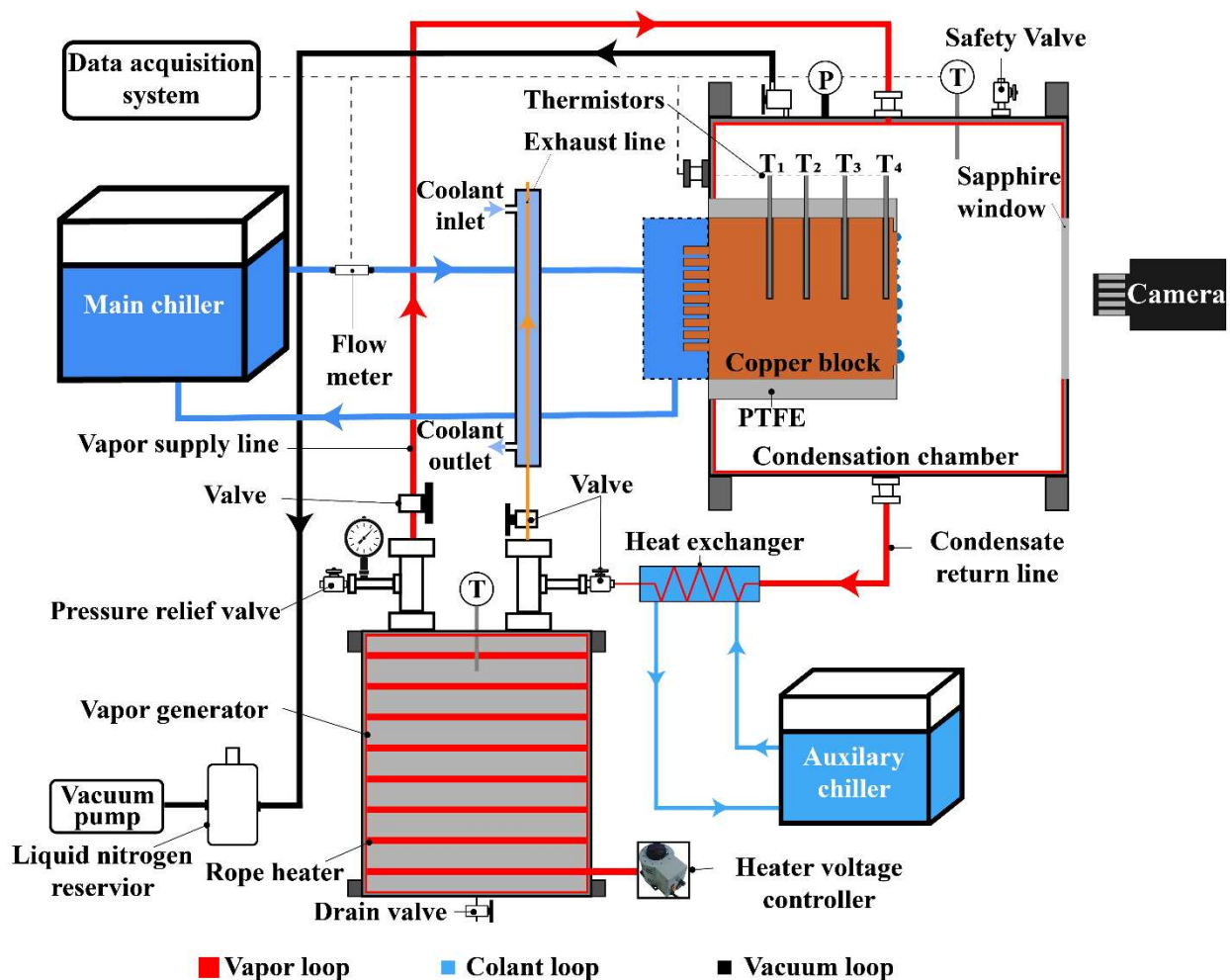


Figure S6. Schematic of the experimental setup for heat transfer measurements. Schematics are not drawn to scale.

A bellows valve (Kurt J. Lesker) was attached to the vapor generator *via* a KF port along the vapor supply line and was used to control the vapor inflow rate to the condensation chamber. A resistance temperature detector (RTD) probe (Evosensors) was fed into the vapor generator *via* a Swagelok fitting that monitored the temperature of the vapor generator. A T-fitting was installed on the vapor generator to integrate a pressure gauge (Bourdon needle dial, IdealVac) and a pressure-relief valve (Pfeiffer) *via* a KF port. The pressure inside the vapor generator was monitored by the pressure gauge, while the pressure relief valve served to protect the system from overpressure by venting excess vapor to the ambient environment.

A secondary stainless steel tube (exhaust line), integrated with an inline counterflow heat exchanger, was connected to the vapor generator. A vapor discharge valve (Ball valve, Idealvac)

was installed along the line *via* a KF adapter port. The exhaust line served two purposes. First, it served as a port that was used to fill the liquid mixtures into the vapor generator through the vapor discharge valve. Second, during the boiling process, the vapor discharge valve was opened to allow the dissolved non-condensable gases to escape the chamber. The inline heat exchanger was connected to a secondary chiller (1175PD Recirculating Chiller, VWR Scientific) and used for condensing the vapor back into the vapor generator so that only the non-condensable gases were removed from the system during boiling. The outlet of the exhaust line was connected to a flexible tube, so that the non-condensable gases and a residue of the vapor escaping the condensing process were discharged into the fume hood. A drain valve was connected to the bottom side of the vapor generator *via* a Swagelok compression fitting to a stainless-steel tube that served as the drain port for the liquid mixture inside the boiler. Another stainless tube connected the bottom port of the condensation chamber (Swagelok) to the vapor generator and served as the condensate return line through gravitational suction. An auxiliary heat exchanger (Brazed Plate Heat Exchanger, Ferroday) was installed along the condensate return line to condense the remaining vapor back to a liquid and enhance the necessary suction.

The custom-designed condensation chamber used for this work (Ancorp) consisted of a cylindrical stainless-steel vessel horizontally seated on a stainless-steel stand (Ancorp) with a sapphire viewing window and apertures for various components. The vapor supply line was fed into the top of the condensation chamber *via* a KF adapter port to supply incoming vapor from the vapor generator. Flexible resistive heaters (Chromalox), powered by a DC power supply (Eventek), and insulation were wrapped around the exterior of the condensation chamber to prevent condensation at the inside wall. The vertical condensation copper block was thermally insulated from the vapor by a polytetrafluoroethylene (PTFE, McMaster-Carr) housing and was mounted against the rear side of the interior of the condensation chamber to serve as a condensation substrate. Two insulated water flow lines (Swagelok tee) were fed into the back side aperture *via* a CF flange (Kurt J. Lesker) to supply cooling water to the chamber from the main chiller (Thermochill II recirculating chiller, Thermoscientific). A flowmeter (Picomag, Endress+Hauser USA) with an accuracy of $\pm 0.8\%$ was installed along the water inflow line.

A 4-way KF fitting (Kurt J. Lesker) was attached to one of the side ports of the condensation chamber. A high-accuracy pressure transducer (728A13TGA2FA Baratron Capacitance

Manometer, MKS) was attached to top port of the 4-way KF fitting to monitor the gas and vapor pressure within the chamber and to determine the saturation pressure. The bottom port of the 4-way KF fitting was attached to a safety valve (Idealvac), which was used to release the chamber to ambient conditions if needed. An RTD probe (Evosensors) was fed through a Swagelok compression fitting on the opposite side of the condensation chambers and monitored the vapor temperature within the chamber.

One flange connected to a stainless-steel bellow hose (Kurt J. Lesker) that served as a vacuum line, which was connected to the vacuum pump (Adixen 2005 dual stage rotary vane, Idealvac) that was used to evacuate the condensation chamber prior to introducing the vapor. A ball valve (Idealvac) was integrated along the vacuum line to isolate the vacuum pump from the chamber and maintain the vacuum once the pump-down process was complete and the pump was turned off. A liquid nitrogen cold trap was also incorporated along the vacuum line to remove any moisture from the gas to protect the pump and to achieve a higher quality vacuum condition.

A 1.25" diameter polished flat copper condensing sample was vertically mounted and pressed against the copper cooling block substrate by the PTFE insulating block to ensure good thermal contact between the copper block and condensing sample. Thermal paste was applied between the interfaces to further improve heat transfer. The chilled water flowed through the water flow lines and impacted the back side of the copper block, which consisted of several equally spaced cylindrical fins to enhance the heat removal process and maintain the test sample at the desired temperature.

Bundles of thermistors were used to measure the temperature inside the condensation block, which was surrounded by the PTFE insulator. Three equally spaced 10 k Ω NTC thermistors (803-USP10975, Mouser electronics) were inserted into the condensing copper block to monitor the temperature. The corresponding temperature readings were used to calculate the 1D condensation heat flux through the copper block. A fourth thermistor (803-USP10975, Mouser electronics) was inserted into the condensing sample to extrapolate the surface temperature. All thermistors were wired to the electrical feedthrough CF flange (EFT0083032, Kurt J.Lesker) and wrapped with PTFE tape and then with shrink tube to shield them from the condensing vapor and minimize noise during measurements. The thermistors were calibrated by immersing them into a circulating bath (AD07R-40, Polyscience) filled with 50/50 water/ethylene glycol, which was held at a constant

temperature to $\pm 0.01^\circ\text{C}$. The thermistors in the water bath were allowed to reach steady state before collecting the calibration data. The readings from the thermistor (x-axis) and the actual/ true water bath temperature (y-axis) of Figure S7 were used as a calibration curve.

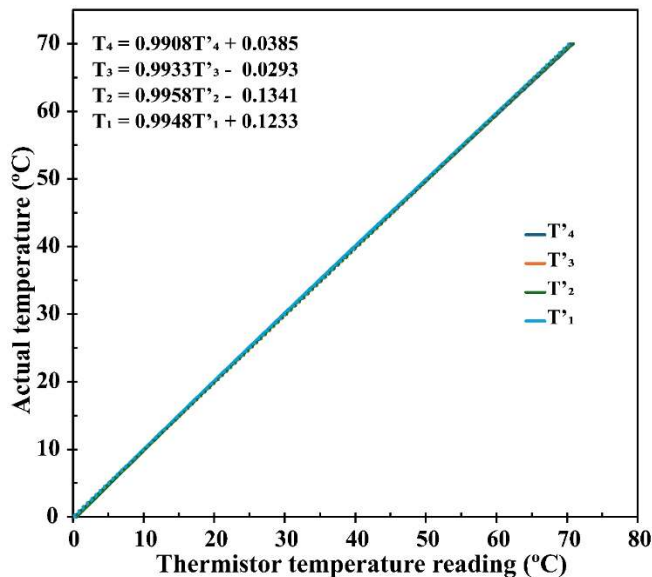


Figure S7. *Thermistor calibration curve. The bundle of thermistors was calibrated prior to the experiment by immersing them in a constant-temperature water/EG bath.*

The thermistor bundles and pressure transducer were electrically connected to the analog input source channel of a data acquisition system (Keysight technologies 34972A), which was interfaced to a computer for data recording. In order to visually record data, a high-speed camera (Photron Mini AX200, Japan)¹⁴ was placed in line with the 1.5” sapphire viewing window on the chamber. In addition, a DSLR camera (Canon T6i) with a macro lens (Canon MP-E 65mm 1-5x Macro), which was interchangeable with the high-speed camera, could be used to obtain color images. Moreover, since the sapphire window is infrared transparent, a thermal camera (Telops M3k) could replace the optical cameras to obtain spatial temperature information of the condensation process.

S8. Experimental procedure

For each experimental trial, a set of strict procedures was followed to ensure consistency throughout the experiments. The first step was to ensure the environmental chamber was thoroughly clean and there were no traces of contamination from prior use. To do so, the chamber setup was filled with coca cola ¹⁵ for at least 8 hours and then drained from the chamber *via* a drain valve. Distilled water was then filled in the chamber and drained several times (8-10) to rinse the

chamber and remove impurities. The next step of the process was to turn on the voltage regulators and power supply to heat up the environmental chamber wall to vaporize any residue of the distilled water used for cleaning and then remove it by turning on the vacuum pump. The hoses from the chamber were disassembled and the internal corrugated were dried using Kimwipes (Kimberly-Clark Professional). The hoses were left to air-dry for at least 24 hours before reassembly to ensure complete moisture removal.

Once the chamber was cleaned and re-assembled, prior to conducting condensation experiments, the voltage regulators and power supplies were turned on to heat up the environmental chamber to prevent condensation on the chamber walls. Next, the vacuum pump down procedure was initiated. First, the liquid nitrogen moisture trap was filled to about three-quarter capacity. The vapor supply valves connecting the vapor generator to the vapor supply line and the condensate return valve connecting the chamber to condensate return line were both fully closed. The ball valve connecting the chamber to the vacuum pump was opened. The vacuum pump was then turned on, initiating the pump-down process. The pressure inside the chamber was monitored during the pump-down process. This process took nearly four hours to achieve the best vacuum level our system can reach. Once the condensation chamber was pumped down to ≈ 280 Pa, the lowest pressure that could be reached in our system, the chamber was isolated from the vacuum pump and the pump was turned off. At one point, the chamber pressure was monitored overnight to characterize the leakage rate (Figure S8). The leak rate was 22.6 Pa/hr during the first 1.5 hours, then increased to approximately 40.5 Pa/hr for the remainder of the test duration.

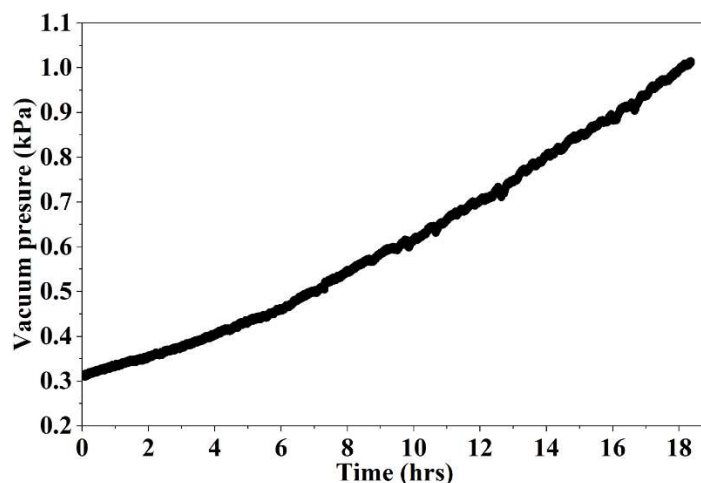


Figure S8. *Overnight leak rate characterization of the condensation chamber.*

During pump down, the setup procedure for the three water flow loops was performed simultaneously, as described below. A high-capacity chiller (Thermochill II recirculating chiller, Thermoscientific) was turned on in order supply the cooling water to the condensation copper block. The chiller output temperature was set between $-10\text{ }^{\circ}\text{C}$ and $30\text{ }^{\circ}\text{C}$ to vary the condensing surface temperature, enabling the collection of heat transfer data over a range of subcooling conditions. The flowrate was monitored with the flowmeter integrated in the cooling water line. A secondary chiller (VWR Scientific), integrated with the parallel heat exchanger in the vapor discharge line that served for condensing back the vapor into the vapor generator so that only the non-condensable gases were removed, was also turned on. In the meantime, the auxiliary chiller (AD07R-40-A11B, Polyscience), integrated with the auxiliary brazed plate heat exchanger along the line of condensate return line, was turned on as well and set to $15\text{ }^{\circ}\text{C}$.

Once the coolant water flow in all chillers reaches steady condition, and after ensuring the vapor supply valve was fully closed, the vapor generator was filled with approximately 4 liters of the mixture of interest through the vapor discharge valve. The rope heater around the vapor generator was turned on with the heater power controller set to maximum output to boil the liquid rigorously. The temperature within the vapor generator was monitored by the installed RTD probe. During the boiling process, the vapor discharge valve was open to remove the dissolved non-condensable gases from the liquid mixtures. Once boiling was achieved and the temperature within the vapor generator was $> 98\text{ }^{\circ}\text{C}$ for at least 10 minutes, the vapor discharge valve was closed.

Prior to beginning the condensation experiments, the DSLR camera was turned on for visual recording of the sample during condensation. Afterwards, the power regulator of the rope vapor generator was manually adjusted to control the pressure inside the vapor generator and the vapor supply valve was slowly opened until the desired saturation pressure in the condensation chamber was reached. Quasi-steady state conditions were typically reached after 2 minutes of full operation. Upon completion of the experimental run, the heaters were first turned off while the cooling water was kept running for several hours to ensure proper cooldown of the system.

S9. Experimental calculations and error propagation

Condensation heat transfer coefficient

The heat transfer coefficient was obtained by first calculating the heat flux (q'') through the condensation copper block using a one dimensional (1D) Fourier heat conduction approximation given by:

$$q'' = -k \frac{dT}{dx} = \frac{Q}{A_1}, \quad (S7)$$

where k is the thermal conductivity of copper (401 W/m.K) and dT/dx is the measured temperature gradient along the copper block. We thermally insulated the copper block using a custom-made PTFE-sleeve, which allows us to utilize the 1D heat transfer approximation. The three thermistors located at pre-determined and equally spaced locations in the copper block measured the temperature, from which the temperature gradient dT/dx was calculated, with A_1 denoting the corresponding cross-sectional area (see Figure S9**Error! Reference source not found.**(a)) and Q the total heat transfer rate. The thermal resistance network represents the total resistance of the test rig, which included the copper sample, thermal paste and copper block. The thickness of the thermal paste was taken as 5 μm and the corresponding thermal conductivity was 4.7 W/m.K. To verify the validity of the 1D heat conduction assumption, the temperature gradients between adjacent thermistors were calculated from the experimental measurements and are plotted in **Error! Reference source not found.**(b). The close agreement among these gradients indicates a nearly linear temperature profile across the sample, thereby confirming that the 1D heat conduction approximation is appropriate.

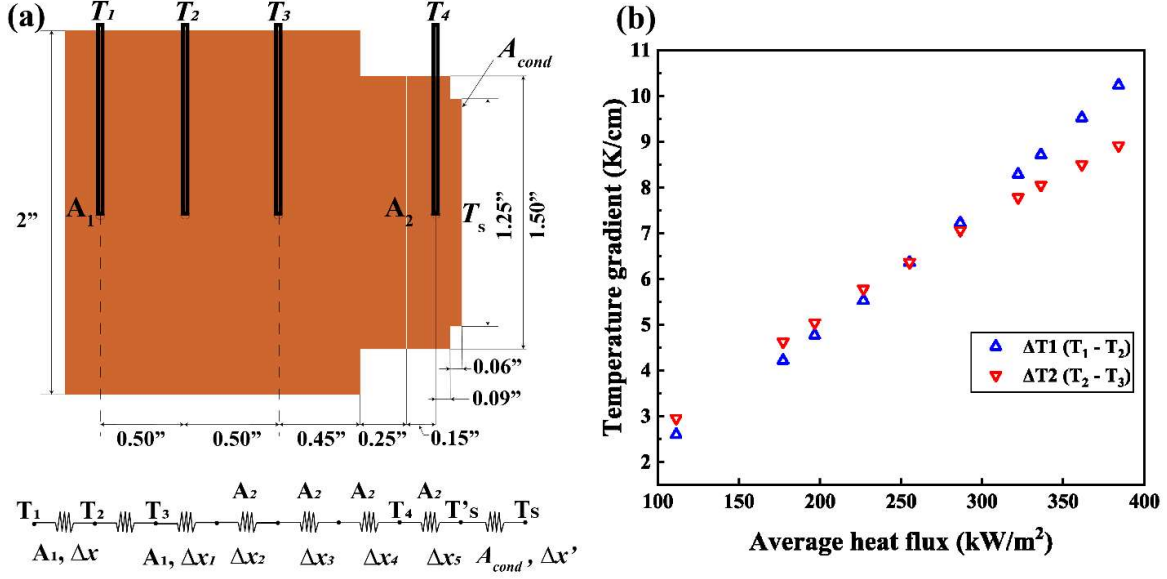


Figure S9. (a) Side-view schematic of condensation copper block with thermistor hole placement and thermal resistance network. (b) A representative measurement showing the temperature gradient per unit distance between two consecutive thermistors.

Based on the energy balance, the condensation heat flux (q''_{cond}) on the surface area (A_{cond}) was calculated as:

$$q''_{cond} = \frac{Q}{A_{cond}} = \frac{q'' A_1}{A_{cond}}. \quad (S8)$$

The temperature of the condensing surface (T_s) could then be determined by assuming 1D heat conduction through the condensing block, as:

$$T_s = T_4 + \frac{q''_{cond} \Delta x'}{k}, \quad (S9)$$

where T_4 is the temperature measured by the thermistor close to the condensing surface and $\Delta x'$ is the distance between the condensing surface and the location of the thermistor.

The surface subcooling temperature (ΔT) is defined as the temperature difference between the saturated vapor (T_{sat}) inside the chamber and the temperature of the condensing surface (T_s),

$$\Delta T = T_{sat} - T_s. \quad (S10)$$

The condensation heat transfer coefficient (h_c) is defined as the ratio of condensation heat flux to surface subcooling, which can be expressed as:

$$h_c = \frac{q''_{cond}}{\Delta T}. \quad (S11)$$

Error propagation analysis

To quantify the uncertainty, $\delta(h_c)$, of our measured condensation heat transfer coefficients (h_c), we combined the known instrumental uncertainties associated with each measured quantity used for calculating the value of h_c . Because h_c is determined from the measured heat flux (q''_{cond}) and the measured subcooling (ΔT), the overall systematic uncertainty of the condensation heat transfer coefficients follows from the propagating the individual errors in these terms, as expressed below

¹⁶ :

$$\delta(h_c) = \sqrt{\left(\frac{\partial h_c}{\partial q''_{cond}} \delta(q''_{cond})\right)^2 + \left(\frac{\partial h_c}{\partial \Delta T} \delta(\Delta T)\right)^2}. \quad (S12)$$

Based on the error propagation, the uncertainty of heat flux $\delta(q)$ was determined by:

$$\delta(q) = \sqrt{\left(\frac{\partial q''_{cond}}{\partial T} \delta(T)\right)^2 + \left(\frac{\partial q''_{cond}}{\partial x} \delta(x)\right)^2}. \quad (S13)$$

The uncertainty of the temperature measurements in the condensation block is subject to a ± 0.4 °C error associated with the thermistor's specification. Additionally, the uncertainty associated with the distance between the pre-drilled holes for the thermistors in the condensation block, $\delta(x)$, was given by the machine shop to be ± 0.003 ".

The uncertainty of the surface subcooling temperature, $\delta(\Delta T)$, was determined by:

$$\delta(\Delta T) = \sqrt{\left(\frac{\partial \Delta T}{\partial T} \delta(T)\right)^2 + \left(\frac{\partial \Delta T}{\partial P} \delta(P)\right)^2}. \quad (S14)$$

Lastly, the uncertainty associated with the subcooling temperature difference (calculated according to eq. (S14) can be attributed to the thermistor error (± 0.4 °C) combined with the uncertainty in

the saturation temperature, $T_{sat}(P_{sat})$, which is directly tied to the uncertainty of the pressure transducer measurement ($\delta(P)$). Our high-pressure transducer (728A13TGA2FA, MKS) has a rated accuracy of $\pm 0.4\%$ given by the manufacturer, allowing us to determine the corresponding saturation temperature. The error bars reported in Figure 5 of the main manuscript were obtained by combining the subcooling temperature error ($\delta(\Delta T)$) with heat flux error ($\delta(q''_{cond})$) according to eq. (S12). Table S2 summarizes the uncertainties associated with each measured quantity.

Table S2. Uncertainties corresponding to the direct experimental measurements

Experimental measurements	Uncertainty (\pm)
Calibrated thermistors	0.4K
Saturated vapor pressure (P_{Sat})	0.5%
Length measurement (x)	0.003''

S10. Filmwise condensation model and setup validation

To model filmwise condensation on a smooth vertical flat Cu substrate, the classical Nusselt model was used, given by ¹⁷:

$$h_{Nu} = 0.943 \left(\frac{\rho_l(\rho_l - \rho_v)g h'_{fg} k_l^3}{\mu_l D \Delta T} \right)^{\frac{1}{4}}, \quad (\text{S15})$$

$$h'_{fg} = h_{fg} + c_{p,l} \Delta T, \quad (\text{S16})$$

where g is the gravitational acceleration (9.81 m/s^2), ρ_l is the liquid density, ρ_v is the vapor density, D is the diameter of the condensing substrate, μ_l is the dynamic viscosity of the condensate, k_l is the thermal conductivity of the condensate, h'_{fg} is the modified latent heat of vaporization accounting for the change in specific heat of condensate, and $c_{p,l}$ is the specific heat of the condensate.

An example of Marangoni and filmwise condensation heat transfer coefficients as a function of condenser subcooling temperature yielded from the above model is plotted in Figure 5 of the main manuscript under typical experimental conditions.

Additionally, to validate the experimental setup, filmwise condensation of pure water was conducted and the measured heat transfer coefficients were compared against the theoretical predictions from the Nusselt model, which showed good agreement (see Figure S10).

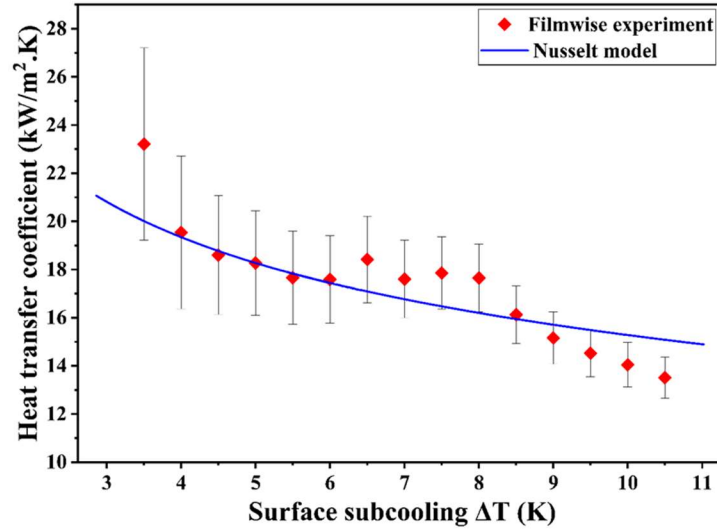


Figure S10. Validation of experimental setup. Measured heat transfer coefficient as a function of surface subcooling compared with classical Nusselt theory for filmwise condensation of pure water.

S11. Time-resolved IR imaging of Marangoni dropwise condensation

Figure S11 shows time-lapse infrared (IR) images obtained during the Marangoni dropwise condensation of a water-EG mixture on the clean smooth copper surface during the initial transient condensate formation stage (see SI, video S3). As expected, when the vapor mixture contacts the condensing surface, small discrete droplets form and rapidly grow by coalescing with the neighboring droplets (see Figure S11(a-e)). Once the size of the droplets is large enough, the droplets are removed from the condensing surface by gravity (see Figure S11(f)). The same behavior is observed during the quasi-steady state operation (see Figure S12 and SI, video S4).

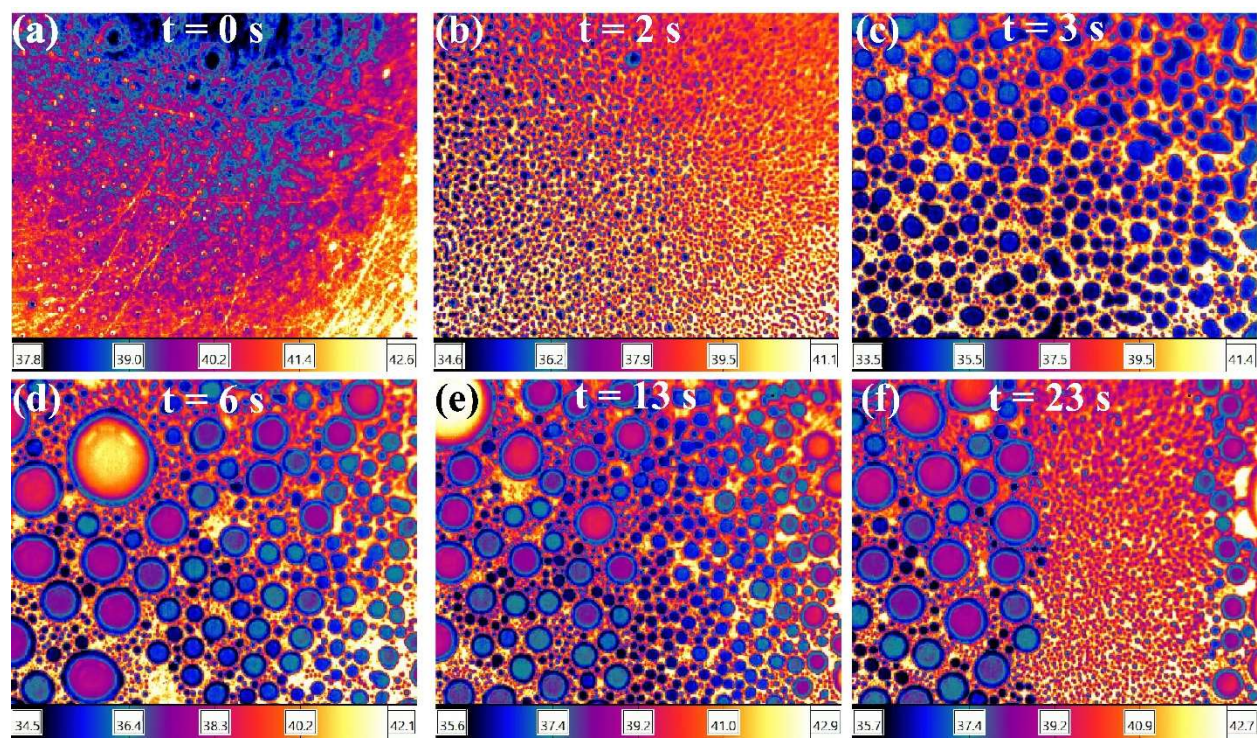


Figure S11. Time-lapse IR images during the initial stages of water-EG mixture condensation.

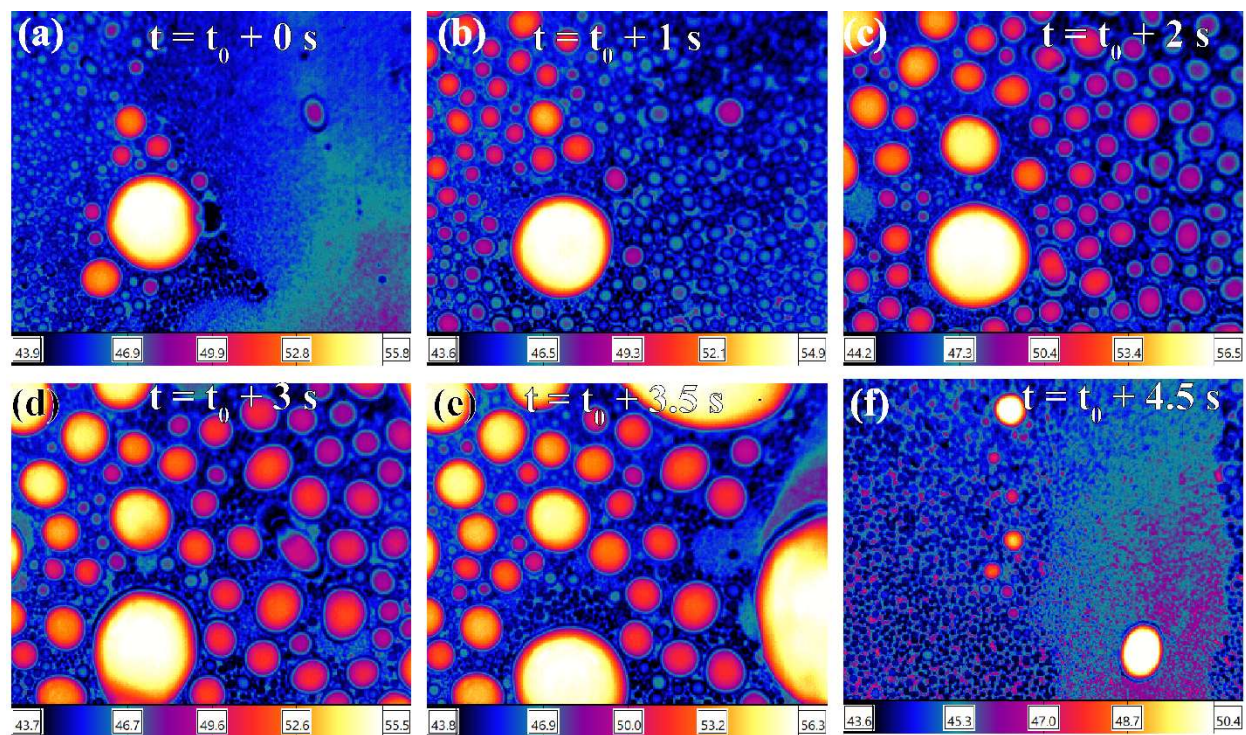


Figure S12. Time-lapse IR images during the quasi-steady state condensation of a water-EG mixture.

References

1. Utaka, Y. & Nishikawa, T. Measurement of Condensate Film Thickness for Solutal Marangoni Condensation Applying Laser Extinction Method. *J Enh Heat Transf* **10**, 119–130 (2003).
2. Oron, A., Davis, S. H. & Bankoff, S. G. Long-scale evolution of thin liquid films. *Rev. Mod. Phys.* **69**, 931–980 (1997).
3. Ford, J. D. & Mcaleer, J. E. Non-filmwise condensation of binary vapors: Mechanism and droplet sizes. *Can J Chem Eng* **49**, 157–158 (1971).
4. Hijikata, K., Fukasaku, Y. & Nakabeppu, O. Theoretical and Experimental Studies on the Pseudo-Dropwise Condensation of a Binary Vapor Mixture. *Journal of Heat Transfer* **118**, 140–147 (1996).
5. Utaka, Y. & Che, Z. Condensate Drop Movement by Surface Temperature Gradient on Heat Transfer Surface in Marangoni Dropwise Condensation. in *An Overview of Heat Transfer Phenomena* (ed. Kazi, M. S. N.) (InTech, 2012). doi:10.5772/51830.
6. AMS 2025.1 COSMO-RS, SCM, Theoretical Chemistry, Vrije Universiteit, Amsterdam, The Netherlands, [http:// www.scm.com](http://www.scm.com).
7. Pye, C. C., Ziegler, T., Van Lenthe, E. & Louwen, J. N. An implementation of the conductor-like screening model of solvation within the Amsterdam density functional package — Part II. COSMO for real solvents. *Can. J. Chem.* **87**, 790–797 (2009).
8. Xiong, R., Sandler, S. I. & Burnett, R. I. An Improvement to COSMO-SAC for Predicting Thermodynamic Properties. *Ind. Eng. Chem. Res.* **53**, 8265–8278 (2014).
9. Shardt, N. & Elliott, J. A. W. Model for the Surface Tension of Dilute and Concentrated Binary Aqueous Mixtures as a Function of Composition and Temperature. *Langmuir* **33**, 11077–11085 (2017).
10. Vargaftik, N. B., Volkov, B. N. & Voljak, L. D. International Tables of the Surface Tension of Water. *Journal of Physical and Chemical Reference Data* **12**, 817–820 (1983).
11. MEGlobal. Monoethylene Glycol (MEG) Technical Product Brochure.
12. The Dow Chemical Company. Triethylene Glycol Material Safety Data Sheet.
13. Ford, J. D. & Missen, R. W. On the conditions for stability of falling films subject to surface tension disturbances; the condensation of binary vapors. *Can J Chem Eng* **46**, 309–312 (1968).
14. Abere, A., Chang, S., Zhao, C., Won, Y. & Weisensee, P. B. Investigation of droplet deformation and breakup dynamics in porous media using machine learning-assisted computer vision. *International Journal of Multiphase Flow* 105675 (2026) doi:10.1016/j.ijmultiphaseflow.2026.105675.
15. Jivani, S. R. Investigation of Marangoni condensation of binary mixtures. (Queen Mary University of London, 2018).
16. Kline, S. J. & McClintock, F. A. Describing Uncertainties in Single-Sample Experiments. *Mechanical Engineering* **75**, 3–8 (1953).
17. Carey, V. P. *Liquid-Vapor Phase-Change Phenomena: An Introduction to the Thermophysics of Vaporization and Condensation Processes in Heat Transfer Equipment*. (CRC Press, Boca Raton, 2020).